

# High Structural Stability and Reaction Mechanism of Porous Carbon Nanobox Encapsulated Monodisperse CoP Nanoparticles for High-Performance Lithium-Ion Battery

Xiang Cui,<sup>[a]</sup> Minxia Liang,<sup>[a]</sup> Lei Wang,<sup>[a]</sup> Longgang Li,<sup>[b]</sup> Qianqian Peng,<sup>[a]</sup> Hanghang Dong,<sup>[a]</sup> Shuo Qi,<sup>[a]</sup> Weiwei Sun,<sup>[a]</sup> Li-ping Lv,<sup>[a]</sup> Xianfei Chen,\*<sup>[b]</sup> Yong Wang,<sup>[a]</sup> Shuangqiang Chen,\*<sup>[a]</sup> and Shulei Chou\*<sup>[c]</sup>

Transition metal phosphides (TMPs) are perplexed by the low electronic/ionic conductivity, volume variations, and unstable reaction interfaces. To tackle these issues, herein, we have proposed a low-temperature phosphorization strategy by reactions between Co-based metal-organic frameworks (MOF) and sodium dihydric hypophosphite to encapsulate monodisperse CoP nanoparticle (~12 nm) into MOF-derived hollow and porous carbon nanobox (CoP@PCB). Compared to bare CoP, such CoP@PCB electrode has shown remarkable electrochemical performance, which is highly ascribed to its robust structural feature, pre-reserved voids, monodisperse CoP nano-

particles, and stable reaction interfaces, as well as fast reaction kinetics. Moreover, the good electrochemical properties of CoP@PCB/LiFePO<sub>4</sub> full cells have demonstrated practical possibility. The formation of Co and Li<sub>3</sub>P as discharged products has corroborated the redox conversion reaction mechanism, as assessed by in-situ X-ray diffractions. The favorable function of the carbon shell in boosting both electronic conductivity and lowering diffusion energy barriers has been confirmed by theoretical calculations, demonstrating an important synergistic effect.

The rechargeable lithium-ion batteries with higher specific energy density, longer cycle life, and better safety have been widely applied as power sources.<sup>[1,2]</sup> Although commercial graphite has been applied in most circumstances, its capacity is hard to meet future market requirements. Transition metal phosphides (TMPs) are recognized as a kind of promising candidates due to their high gravimetric capacities, high thermal stability as well as low cost.<sup>[3,4]</sup> The lithium storage mechanism of TMPs is mainly based on the conversion reactions:  $MP_x + 3xLi^+ + 3xe^- \leftrightarrow M + xLi_3P$  ( $M = \text{transition metal}$ ).<sup>[5-11]</sup> Many metal phosphide composites, including self-adaptive FeP@C nanocages,<sup>[12]</sup> CoP@C hybrids,<sup>[3,13,14]</sup> Sn<sub>4</sub>P<sub>3</sub>-NC,<sup>[15]</sup> CuP<sub>2</sub>/C,<sup>[16]</sup> and Ni<sub>2</sub>P@C<sup>[17]</sup>, have been reported as

anodes for lithium-ion batteries (LIBs), demonstrating enhanced electrochemical performance compared with pure metal phosphides. Among them, CoP with a theoretical capacity of 895.4 mAh g<sup>-1</sup> is regarded as the most promising candidate for LIBs. However, similar to other TMPs, CoP is also largely hampered by many aspects, including irreversible capacity loss, sluggish ion/electron mobility, huge volumetric expansion, and unstable reaction interfaces.<sup>[18,19]</sup> Different carbon materials are applied as conductive backbones to support semi-conductive CoP for enhanced electrochemical performances.<sup>[20]</sup> As far as large volume changes, pre-reserved internal voids are of significant importance to stabilizing solid electrolyte interface (SEI) and maintaining a good physical connection.<sup>[21]</sup> Moreover, the decrease in particle size can not only increase specific surface area but also enhance its electrochemical activity and reaction kinetics.<sup>[22]</sup> Even though much attractive progress has been made, such as CoP@NC-CNT composite,<sup>[23]</sup> CoP@carbon nanotube,<sup>[24]</sup> and 3D CoP/r-GO nanocomposite,<sup>[25]</sup> but challenges still remain.

To tackle these problems, herein, we synthesized the Co-based metal-organic frameworks (Co-based MOF) derived porous carbon nanobox encapsulating monodisperse CoP (CoP@PCB) composites with high structural stability and pre-reserved voids by a low-temperature phosphorization strategy of reactions between Co-based MOF and sodium dihydric hypophosphite. Such CoP@PCB has displayed completely physical encapsulation to confine volume variations of CoP, hollow and porous carbon shells with multi-channels for ionic diffusion, making it possible to maintain high structural stabilization and superior physical contact. Figure 1 displays the

[a] X. Cui, M. Liang, L. Wang, Q. Peng, H. Dong, S. Qi, W. Sun, L.-p. Lv, Y. Wang, Prof. Dr. S. Chen  
Department of Chemical Engineering, School of Environmental and Chemical Engineering  
Shanghai University  
No. 99 Shangda Road, Shanghai, 200444, P. R. China  
E-mail: chensq@shu.edu.cn

[b] L. Li, X. Chen  
College of Materials and Chemistry & Chemical Engineering  
Chengdu University of Technology  
Chengdu 610059, P. R. China  
E-mail: chenxianfei2014@cdut.edu.cn

[c] S. Chou  
Institute for Carbon Neutralization, College of Chemistry and Materials Engineering  
Wenzhou University  
Wenzhou, Zhejiang 325035, China  
E-mail: chou@wzu.edu.cn

 Supporting information for this article is available on the WWW under  
<https://doi.org/10.1002/batt.202200271>

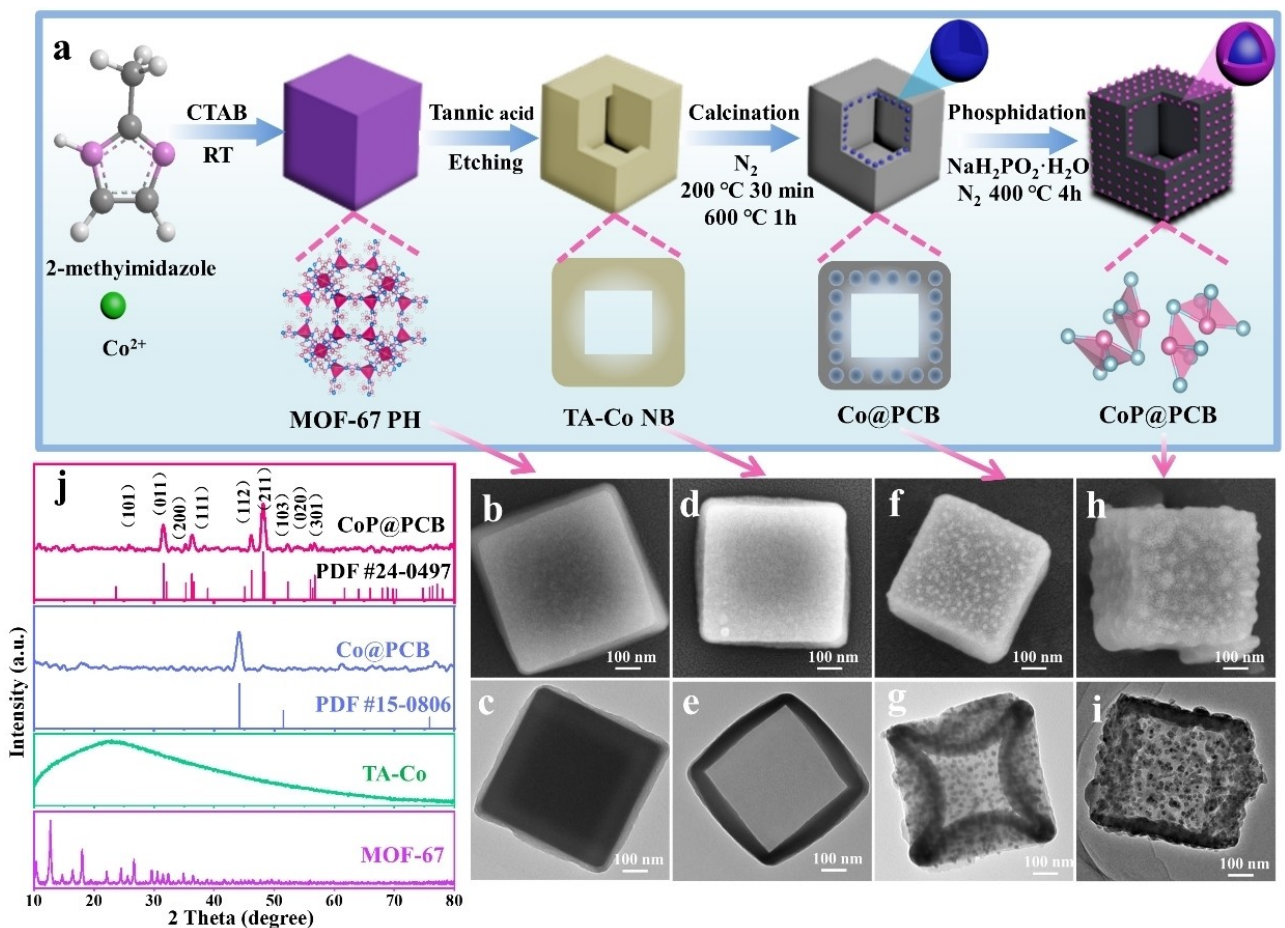


**Figure 1.** Schematic illustration of the porous carbon nanobox encapsulated monodisperse CoP nanoparticles and characterization of the intermediate materials: a) schematic illustration of the synthesis process of the CoP@PCB. b, d, f, h) SEM and c, e, g, i) TEM images of b, c) MOF-67 PH, d, e) TA-Co NB, f, g) Co@PCB, h, i) CoP@PCB, and j) XRD patterns of all samples.

schematic synthesis process and the morphology characterizations, and more details are shown in Supporting Information (Figures 1a–i, S1–S3 in Supporting Information). Monodisperse CoP@PCB composites were obtained with three typical structural features in Figure 1(h and i): i) average particle size of 12 nm for CoP, ii) huge internal voids (~400 nm in width) in the carbon nanobox, and iii) thin and porous carbon shell. Without the assistance of MOF-67 and tannic acid etching, bare CoP, obtained in the same process, only displays a large nanosheet structure (Figures S4 and S5). As shown in Figure 1(j), all the XRD peaks of CoP@PCB are well assigned to the orthogonal CoP (PDF #24-0497) without any impurities, indicating the successful phase transformation. Similarly, bare CoP synthesized through the same procedure was also in the pure phase (Figure S6).

The high-resolution transmission electron microscope (HRTEM) images have confirmed that monodisperse CoP NPs, with an average particle size of ~12 nm in a narrow range by statistics calculation, are well confined into porous carbon shells (~22 nm in thickness), forming a homogenous CoP distribution and completely physical encapsulation in the hollow and porous carbon nanobox derived from Co-based MOF as shown in Figures 2(a and b) and S7. Those pre-reserved

voids stem from the pyrolysis of MOF-67 structure and chemical etching by tannic acid. The lattice fringe with a spacing of 0.283 nm in Figure 2(c) is corresponding to the (011) crystal plane of CoP. The selected area electron diffraction (SAED) pattern in Figure 2(d) can precisely confirm the orthorhombic phase of CoP, referring to (011), (102), (103), and (301) planes. Furthermore, the corresponding elemental mapping images (Figure 2e–h) reveal the uniform distributions of C, Co, and P, respectively. The surface area and pore size distribution were examined by the nitrogen adsorption/desorption method in Figures 2(i) and S8(a). The isotherm curve shows typical type IV isothermal characteristics with an apparent hysteresis ring for mesoporous materials. The specific surface area of the CoP@PCB composite is ~177.7 m<sup>2</sup>g<sup>-1</sup>, which is much higher than that of bare CoP (~4.3 m<sup>2</sup>g<sup>-1</sup>). The mesopores and high surface area of CoP@PCB will facilitate the permeation of the electrolyte and ionic diffusions in Figure S8(a).

To further determine the surface composition of CoP@PCB, X-ray photoelectron spectroscopy (XPS) was analyzed (Figures 2j and S8b–d), exhibiting no impurity elements. Figure S8(b) shows the high-resolution spectrum of C 1s, which is deconvoluted into two peaks at binding energies of 284.8 and 286.3 eV, corresponding to C–C & C=C and C–O, respectively.<sup>[26]</sup>

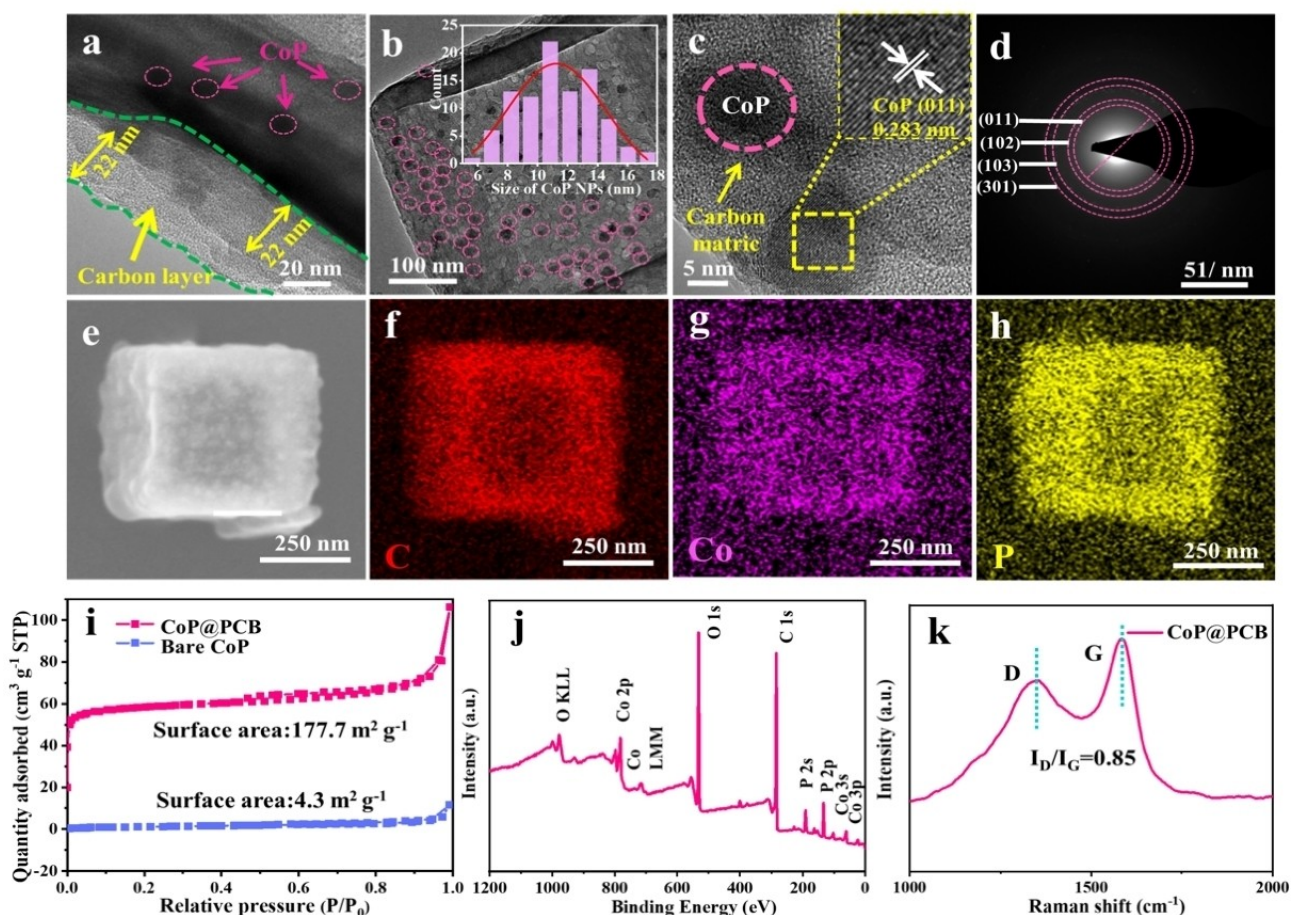


**Figure 2.** Characterization of the CoP@PCB and bare CoP: a–c) HRTEM images (inset of size distribution histogram of the CoP NPs), d) SAED, and e–h) element mapping images. The feature comparisons of i) N<sub>2</sub> adsorption/desorption isotherms, j) full XPS spectrum, and k) Raman spectrum.

The high-resolution P 2p spectrum in Figure S8(c) can be deconvoluted into two different peaks of P–O (133.8 eV) and P 2p<sub>3/2</sub> (129.6 eV) owing to the partial surface oxidations during the test. Besides, the high-resolution spectrum of the Co 2p region is contributed by two peaks of Co 2p<sub>1/2</sub> and Co 2p<sub>3/2</sub> (Figure S8d), respectively.<sup>[27,28]</sup> Figure 2(k) shows the Raman spectra of CoP@PCB with two characteristic peaks located at 1364 and 1585 cm<sup>-1</sup>, corresponding to the D and G bands of carbon, respectively.<sup>[29,30]</sup> The calculated peak intensity ratio between the D and G bands ( $I_D/I_G$ ) is approximately 0.85, indicating that the carbon in the composite is partially graphitic.<sup>[31]</sup>

Figure 3(a) shows the cyclic voltammetry (CV) profiles of the CoP@PCB electrode in the first four cycles at 0.1 mVs<sup>-1</sup>.<sup>[32]</sup> And the detailed analysis is shown in Supporting Information (Figure S9). Figure 3(b) exhibits the typical charge/discharge curves of the CoP@PCB electrode in the 1<sup>st</sup>, 5<sup>th</sup>, 100<sup>th</sup>, and 200<sup>th</sup> cycles at 0.2 A g<sup>-1</sup>. In these curves, the initial reversible capacity of the CoP@PCB is 809 mAh g<sup>-1</sup> with Coulombic efficiency (CE) of 64.5%, mainly attributed to the formation of the SEI layer and the decomposition of the electrolyte.<sup>[33–36]</sup> Even though there is irreversible capacity loss, the reversible capacity (821 mAh g<sup>-1</sup>) of the CoP@PCB electrode is still much higher than bare CoP (378 mAh g<sup>-1</sup>) after 200 cycles (inset in

Figures 3b and S9b). Moreover, the CoP@PCB electrode shows a capacity-increasing phenomenon from 810 mAh g<sup>-1</sup> (the 2<sup>nd</sup> cycle) to 821 mAh g<sup>-1</sup> (the 200<sup>th</sup> cycle) at 0.2 A g<sup>-1</sup> in Figure 3(c), resulting from a capacity active process and well-designed structure as well as high conductivity. The CoP@PCB electrode in Figure 3(d) has also shown outstanding rate capability (1020, 780, 664, 597, 542, and 482 mAh g<sup>-1</sup> at current densities of 0.1, 0.2, 0.5, 1, 2, and 5 A g<sup>-1</sup>, respectively). More importantly, when the current density is back to 0.1 A g<sup>-1</sup>, the reversible capacity can be recovered to 795 mAh g<sup>-1</sup>, demonstrating an excellent reversible capability and high current density tolerant capability.

Moreover, to measure the lithium diffusion coefficient ( $D_{Li^+}$ ), the galvanostatic intermittent titration technique (GITT) was performed at 0.2 A g<sup>-1</sup>. The  $D_{Li^+}$  is calculated by the equation<sup>[37]</sup> as follows:

$$D_{Li^+} = \frac{4}{\pi\tau} \left( \frac{m_B V_M}{M_B S} \right)^2 \left( \frac{\Delta E_s}{\Delta E_t} \right)^2$$

where  $\tau$  represents the constant titration time,  $m_B$ ,  $V_M$ , and  $M_B$  are the weight, molar volume, and molar mass of the active substance, respectively.  $S$  is the electrode's surface area,  $\Delta E_s$  is steady-state voltage change under current disturbance, and  $\Delta E_t$

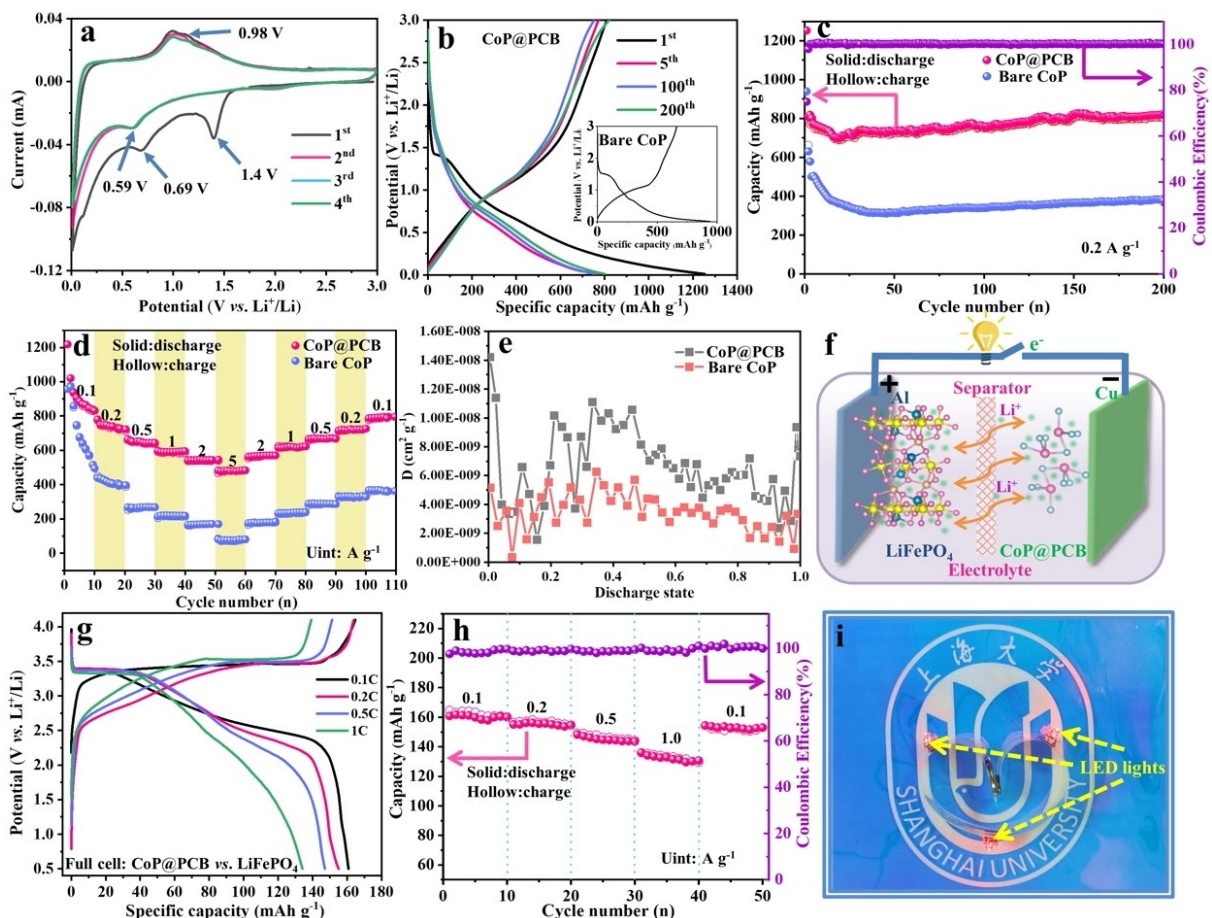


**Figure 3.** Electrochemical performances of the CoP@PCB and bare CoP: a) CV profiles at  $0.1 \text{ mV s}^{-1}$ , b) charge-discharge curves (inset of bare CoP), c) cycling performances at  $0.2 \text{ A g}^{-1}$ , d) rate capabilities, and e) lithium diffusion coefficient values. Electrochemical performance of full cells (CoP@PCB//LFP): f) schematic of the CoP@PCB//LFP full cell, g) electrochemical behaviors of full cells, h) rate capability, and i) optical image showing a single cell powering a 3D-printed flexible bracelet with three red LED lights.

is the total voltage variation. During the discharge process, the  $D_{\text{Li}^+}$  value of the CoP@PCB electrode, calculated by equation, in Figures S10(a) and 3(e) is around  $1.42 \times 10^{-8} \text{ cm}^2 \text{s}^{-1}$  and fluctuated around  $10^{-8} \text{ cm}^2 \text{s}^{-1}$ , which is higher than that of bare CoP ( $\sim 10^{-9} \text{ cm}^2 \text{s}^{-1}$ ). That is associated with the well-built hollow and porous carbon nanobox and monodisperse feature of CoP nanoparticles as well as high structural stability of CoP@PCB composites.

To substantiate the practical feasibility of CoP@PCB, it was assembled with commercial LiFePO<sub>4</sub> (LFP) to construct full cells as schematically shown in Figure 3(f). Figure S10(b) depicts typical charge-discharge profiles of half cells. According to the actual capacities of CoP@PCB and LFP, the mass load ratio between anode and cathode was set at 1: 5 (0.5–4.0 V). The full cell was firstly charged to 4.0 V to activate it, and then it delivered a rechargeable capacity of  $164.8 \text{ mAh g}^{-1}$  at  $0.1 \text{ A g}^{-1}$  with CE of 97.5% (Figure 3g). The irreversible capacity is probably related to the formation of the cathode electrolyte interface (CEI) on the cathode side. When performed rate tests (Figure 3h), the full cell delivered high capacities at different current densities ( $160.8 \text{ mAh g}^{-1}$  at  $0.1 \text{ A g}^{-1}$ ,  $155.1 \text{ mAh g}^{-1}$  at  $0.2 \text{ A g}^{-1}$ ,  $148.2 \text{ mAh g}^{-1}$  at  $0.5 \text{ A g}^{-1}$ , and  $136.1 \text{ mAh g}^{-1}$  at

$1 \text{ A g}^{-1}$ , respectively). More importantly, when the current density was back to  $0.1 \text{ A g}^{-1}$ , the reversible capacity was recovered to  $154.3 \text{ mAh g}^{-1}$ , demonstrating an astonishing rate tolerance capability. The cycle endurances are displayed in Figure S10(c) in 100 cycles, giving comparable capacity retention ratios of 80.2% at  $0.1 \text{ A g}^{-1}$ . To prove the potential in practical usage, a single full cell can power a 3D-printed flexible bracelet with three red LED lights in Figure 3(i) for 2 days, displaying astonishing application possibilities.

To further analyze the reaction mechanism of CoP@PCB composite, it was assembled with Li foil in a specially designed cell using a piece of pure beryllium foil as both the current collector with a mass loading of  $\sim 2 \text{ mg}$  and the scan window for X-ray via a reflecting mode at a current density of  $0.1 \text{ A g}^{-1}$ . As shown in Figure S12(a), the diffraction peak intensities of CoP@PCB are gradually decreased and further fully disappeared during the discharge process, and then they have witnessed an increasing tendency during the charging process, verifying a full phase transformation process. The two-dimensional rainbow contour maps in Figure 4(a) is vividly showing the changes in peak intensities, especially the peak at  $48^\circ$ . That is associated with the reversible conversion reaction between CoP with Li<sup>+</sup>

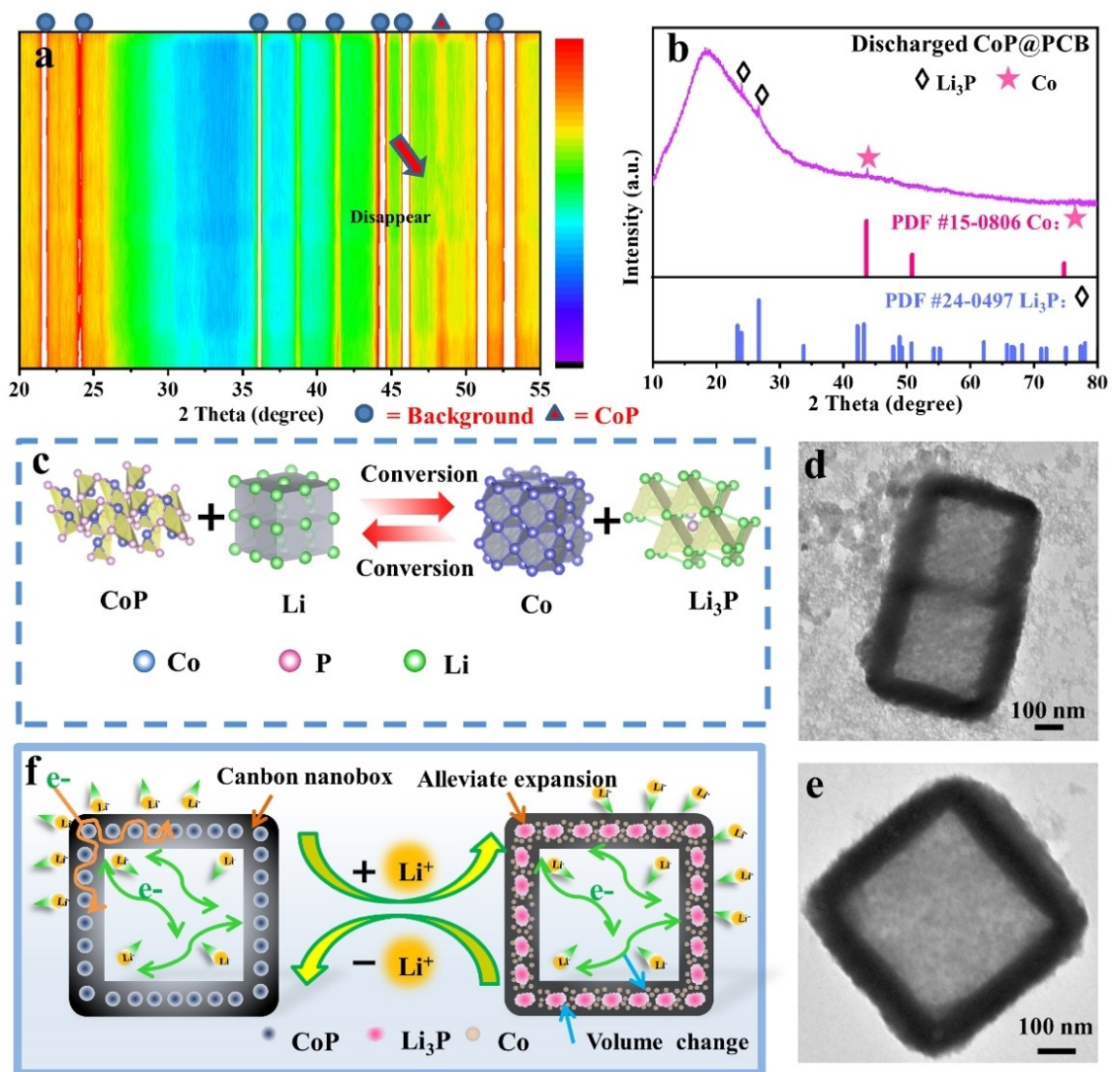


**Figure 4.** a) In-situ XRD patterns (2-dimensional rainbow contour maps) of CoP@PCB anode during 1<sup>st</sup> discharge/charge cycle, b) the ex-situ XRD pattern of the lithiated CoP@PCB anode (discharged to 0.01 V, displaying the discharge products of Co and Li<sub>3</sub>P), and c) the crystal structures of reaction process between CoP and Li. TEM images of the cycled CoP@PCB electrodes: d, e) after 200 cycles at 1.0 A g<sup>-1</sup>, and f) schematic structural features on volume change and transportation paths of Li<sup>+</sup> ion and electrons.

ions ( $\text{CoP} + 3\text{Li}^+ + 3\text{e} \leftrightarrow \text{Li}_3\text{P} + \text{Co}$ ). The diffraction peaks of the discharged products, measured by ex-situ XRD, in Figure 4(b) are well indexed to the standard samples of Li<sub>3</sub>P (24-0497) and Co (15-0806), which also confirms the redox reactions between CoP and Li<sup>+</sup> ions.

To verify the structural stability, post-mortem analyses have been applied to characterize the morphology changes of the CoP@PCB and bare CoP after many cycles. Compared with the fresh CoP nanoplates, the bare CoP electrode has gradually shown many cracks in the plane after 50 and 200 cycles in Figure S13, experiencing huge inner stress. In contrast, the CoP@PCB nanocomposites, with the features of robust structural stability, pre-preserved voids and monodispersed nanoparticles, have shown the stable structure and thin SEI layer on the hollow and porous carbon nanobox in Figure S14(a-d), displaying no cracks and particle aggregations in the carbon nanobox, and robust mechanical stability after 200 cycles

(Figure 4d and e). In short, the outstanding cycling stability and excellent rate performance of CoP@PCB are attributed to the complete physical encapsulation, pre-preserved voids, robust carbon nanobox framework, and monodisperse CoP nanoparticles of the electrode in Figure 4(f). For a single reaction unit, every CoP@PCB composite with such advantages provides ideal places allowing the fast electron transfer and ionic diffusion, effectively confining the volume variations and shortening the Li<sup>+</sup> ion's diffusion path, as well as maintaining a thin SEI layer.

To further understand the different intercalations between bare CoP and carbon-coated CoP (CoP@PCB) electrode as well as Li<sub>3</sub>P (the discharged product) with and without carbon shells, theoretical calculations were performed with simulated crystal structures and graphene(G) as carbon shell to simulate the real electrodes. The main crystal faces of CoP(011) and Li<sub>3</sub>P(001) were selected as examples to carry out the calculation. The top

and side views of the relaxed structures of CoP(011), CoP(011)/G, Li<sub>3</sub>P(001), and Li<sub>3</sub>P(001)/G are demonstrated in Figure S15(a-d), respectively. According to the DFT results, the interactions between the CoP(011) and graphene carbon belong to the Van Der Waals bonding with binding energy ( $E_b$ ) of -0.09 eV and a similar phenomenon happens to Li<sub>3</sub>P(001)/G with an  $E_b$  of -0.18 eV. Moreover, the electron accumulation and depletion in Figure S15(b, d) show two opposite electron transfer directions to graphene, performing as an electron transfer reservoir. When lithiating, the electron is inclined to transfer from graphene to CoP(011) crystal plane. When de-lithiating, the electron is prone to move back to graphene's surface from Li<sub>3</sub>P(001). The electron transfer channel enabled by the robust carbon framework and the evident charge exchange between the graphene carbon and CoP(011)/Li<sub>3</sub>P jointly facilitate the

lithiation, which is beneficial to weakening the polarization phenomenon and reducing irreversible capacity loss in bare CoP. To further investigate the role played by graphene, the total densities of states (TDOS) of the CoP(011) and CoP(011)/G, Li<sub>3</sub>P(001) and Li<sub>3</sub>P(001)/G are calculated as shown in Figure 5(a and b), showing the area of CoP(011)/G encircled by the yellow curve at Fermi level is slightly wider than CoP(011), implying a positive role in the electronic conductivity. Moreover, the Li<sub>3</sub>P(001) is exhibiting a typical semiconductor feature by a wide gap at the Fermi level in Figure 5(b), but Li<sub>3</sub>P(001)/G in the red curve displayed a continuous line at the forbidden band, implying a largely increased electronic conductivity for the carbon-coated discharged product compared to Li<sub>3</sub>P(001). These results are in line with the inner electrochemical resistance results in Figure S12(b). Due to these positive effects,

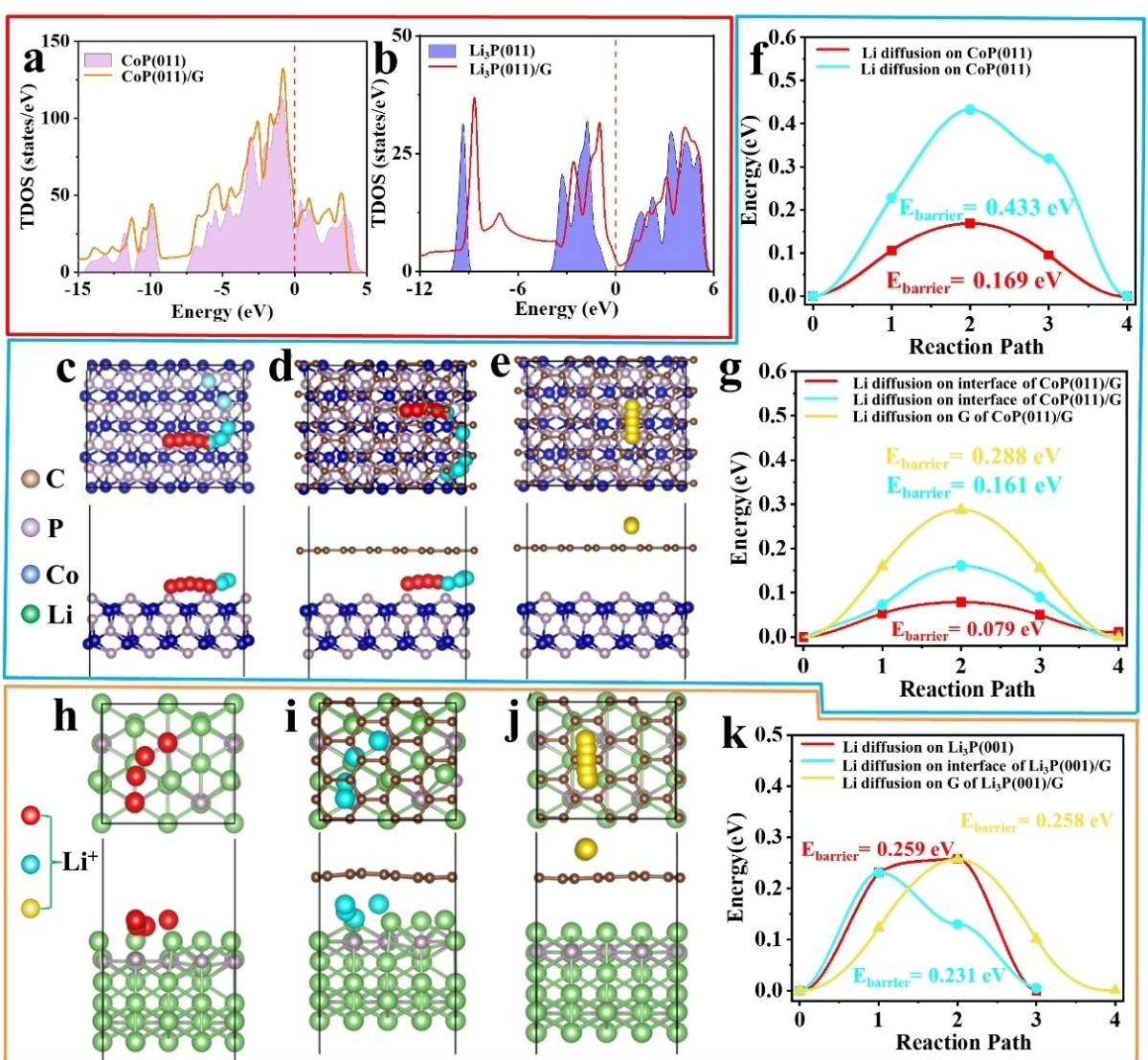


**Figure 5.** Total density of states (TDOS) of a) the CoP(011) and CoP(011)/G(graphene) and b) Li<sub>3</sub>P(001) and Li<sub>3</sub>P(001)/G(graphene). Schematics of the possible migration pathway of Li-ion on c) CoP(011), d) CoP(011)/G(graphene) interface, and e) the graphene side of CoP(011)/G, respectively, and the corresponding energy profile for Li-ions migration along the specific paths in f) CoP(011) and g) CoP(011)/G. Schematics of the possible migration pathway of Li-ion on h) Li<sub>3</sub>P(001), i) Li<sub>3</sub>P(001)/G interface, and j) the graphene side of Li<sub>3</sub>P(001)/G. k) The corresponding energy profile for Li-ions migration along the specific paths in Li<sub>3</sub>P(001) and Li<sub>3</sub>P(001)/G. Gray, silver, blue, and green balls represent C, P, Co, and Li atoms, respectively. The moving Li-ions are highlighted by red, cyan, and golden spheres, respectively.

it is convinced that the enhancement of electronic conductivity of CoP(011)/G and Li<sub>3</sub>P(001)/G is attributed to the positive role played by graphene.

To analyze the mass transfer process of Li-ion on CoP(011) and CoP(011)/G as shown in Figure 5(c–e) (Li<sup>+</sup> ion is moving on the surface or their interface), two typical diffusion directions (horizontal-vertical in the top view) are selected to reveal the diffusion resistance of Li<sup>+</sup> ions. The energy barrier in CoP(011)/G (0.079 eV, where Li<sup>+</sup> ion is moving between the two planes) is much lower than those of the bare CoP(011) (0.169 eV, where Li<sup>+</sup> ion is moving on the surface) in Figure 5(f and g), implying the migration of Li<sup>+</sup> ions in CoP(011)/G is much easier than that of bare CoP(011), agreeing well with the lithium diffusion coefficient of CoP@PCB in Figure 3(f). The lower energy barrier indicates the better the Li<sup>+</sup> diffusion kinetics, which can effectively enhance the electrochemical kinetic performance.<sup>[38,39]</sup> The diffusion energy barrier of Li-ion on G is also calculated (0.288 eV), which is lower than that of CoP(011) (0.433 eV), rationalizing the observed high rate capability of CoP@PCB. Concerning the Li-ion transfer in the discharged products, a typical migration route with lithium-ion diffusing from its most energetic site to its nearest equivalent one is indicated in Figure 5(h–j). With the assistance of graphene, the diffusion energy barrier of Li<sup>+</sup> ions on Li<sub>3</sub>P(001)/G is slightly lower than that of Li<sub>3</sub>P, implying a good synergy effect between Li<sub>3</sub>P and graphene (Figure 5k). Even on the graphene surface, the diffusion energy barrier (0.258 eV) is still comparable with that of bare Li<sub>3</sub>P. Based on those theoretical calculations, it is rationally concluded that the introduction of carbon in the CoP and Li<sub>3</sub>P system is benefiting to enhance its electronic conductivity and lowering the diffusion energy barrier on both surface and interlamellar structure, and the diffusion energy barriers of Li<sup>+</sup> ions on graphene are lower than those of bare crystal systems.

In summary, using a low-temperature phosphorization strategy, monodisperse CoP nanoparticles were homogeneously encapsulated in MOF-derived hollow and porous carbon nano-boxes, allowing for the formation of CoP nanoparticles in a narrow particle distribution range (~12 nm) and complete physical encapsulation with sufficient pre-reserved voids. Compared to bare CoP electrode, CoP@PCB electrode has shown high reversible capacity (820 mAh g<sup>-1</sup> after 200 cycles at 0.2 A g<sup>-1</sup>), and outstanding rate capability (up to 5 A g<sup>-1</sup>), resulting from its completely physical encapsulation for high electronic conductivity, and robust structure of carbon nano-box with hollow and porous features for confining volume variations of monodisperse CoP nanoparticles, stable reaction interfaces, and fast reaction kinetics. Furthermore, the outstanding results of CoP@PCB//LFP full cells have proved the feasibility of the practical application. By detecting the discharged products of Co and Li<sub>3</sub>P, both in-situ and ex-situ X-ray diffraction techniques have confirmed the conversion reaction mechanism of CoP@PCB composite. The beneficial role of the carbon shell in increasing electronic conductivity and decreasing diffusion energy barriers on both the surface and interlamellar structure of CoP and Li<sub>3</sub>P has been well supported by theoretical calculations, revealing a significant synergistic effect.

As a result, such a strategy can be extended to synthesize novel materials for rechargeable batteries or fuel cells.

## Acknowledgements

The authors gratefully acknowledge the National Natural Science Foundation of China (21975154, 22179078), Shanghai Municipal Education Commission (Innovation Program: 2019-01-07-00-09-E00021), and Innovative Research Team of High-level Local Universities in Shanghai. The authors thank Laboratory for Microstructures, Instrumental Analysis, and Research Center of Shanghai University for offering access to material characterizations, and all the computations were performed on the high-performance computing platform of Shanghai University with official permissions.

## Conflict of Interest

The authors declare that they have no known competing financial interests or personal relationships that could have appeared to influence the work reported in this paper.

## Data Availability Statement

The data that support the findings of this study are available from the corresponding author upon reasonable request.

**Keywords:** in-situ XRD • lithium-ion battery • metal-organic framework • monodisperse CoP • theoretical calculations

- [1] J. Wu, S. Liu, F. Han, X. Yao, C. Wang, *Adv. Mater.* **2021**, *33*, 2000751–2000781.
- [2] J. Wu, L. Shen, Z. Zhang, G. Liu, Z. Wang, D. Zhou, X. Yao, *Electrochim. Energy Rev.* **2021**, *4*, 101–135.
- [3] J. Bai, B. Xi, H. Mao, Y. Lin, X. Ma, J. Feng, S. Xiong, *Adv. Mater.* **2018**, *30*, 1802310–1802318.
- [4] N. Wang, Z. Bai, Z. Fang, X. Zhang, X. Xu, Y. Du, L. Liu, S. Dou, G. Yu, *ACS Materials Lett.* **2019**, *1*, 265–271.
- [5] J. Cabana, L. Monconduit, D. Larcher, M. R. Palacin, *Adv. Mater.* **2010**, *22*, 170–192.
- [6] H. Cheng, J. G. Shapter, Y. Li, G. Gao, *J. Energy Chem.* **2021**, *57*, 451–468.
- [7] W. Qi, J. G. Shapter, Q. Wu, T. Yin, G. Gao, D. Cui, *J. Mater. Chem. A* **2017**, *5*, 19521–19540.
- [8] Q. Peng, C. Guo, S. Qi, W. Sun, L. Lv, F. Du, B. Wang, S. Chen, Y. Wang, *RSC Adv.* **2021**, *11*, 1261–1270.
- [9] S. Chen, L. Shen, P. A. van Aken, J. Maier, Y. Yu, *Adv. Mater.* **2017**, *29*, 1605650–1605657.
- [10] D. Xu, M. Liang, S. Qi, W. Sun, L. P. Lv, F. H. Du, B. Wang, S. Chen, Y. Wang, Y. Yu, *ACS Nano* **2021**, *15*, 47–80.
- [11] P. Jing, Q. Wang, B. Wang, M. Xiang, H. Jiang, Y. Zhang, Y. Wei, Y. Zhang, H. Wu, H. Liu, *Ceram. Int.* **2019**, *45*, 216–224.
- [12] P. Zhou, Q. An, S. Zhu, K. A. Owusu, Q. Li, L. Mai, *Chem. Eng. J.* **2020**, *395*, 125124–125132.
- [13] C. Yao, J. Xu, Y. Zhu, R. Zhang, Y. Shen, A. Xie, *Appl. Surf. Sci.* **2020**, *513*, 10800–10805.
- [14] X. Wang, Z. Na, D. Yin, C. Wang, Y. Wu, G. Huang, L. Wang, *ACS Nano* **2018**, *12*, 12238–12246.
- [15] Z. Liu, J. Chen, X. Fan, Y. Pan, Y. Li, L. Ma, H. Zhai, L. Xu, *J. Alloys Compd.* **2021**, *871*, 159531–159541.

- [16] S. O. Kim, A. Manthiram, *ACS Appl. Mater. Interfaces* **2017**, *9*, 16221–16227.
- [17] J. Zheng, X. Huang, X. Pan, C. Teng, N. Wang, *Appl. Surf. Sci.* **2019**, *473*, 699–705.
- [18] J. Jiang, K. Zhu, Y. Fang, H. Wang, K. Ye, J. Yan, G. Wang, K. Cheng, L. Zhou, D. Cao, *J. Colloid Interface Sci.* **2018**, *530*, 579–585.
- [19] S. Fang, D. Bresser, S. Passerini, *Adv. Funct. Mater.* **2019**, *10*, 1902485–1902506.
- [20] W. H. Qiu, G. Zhang, S. G. Lu, Q. G. Liu, *Solid State Ionics* **1999**, *121*, 73–77.
- [21] H. K. Liu, G. X. Wang, Z. P. Guo, J. Z. Wang, K. Konstantinov, *J. New Mater. Electrochem. Syst.* **2007**, *10*, 101–104.
- [22] M. Fan, D. Liao, M. F. A. Aboud, I. Shakir, Y. Xu, *Angew. Chem. Int. Ed.* **2020**, *59*, 8247–8254; *Angew. Chem.* **2020**, *132*, 8324–8331.
- [23] M. Chen, P. Zeng, Y. Zhao, Z. Fang, *Front. Mater.* **2018**, *12*, 214–224.
- [24] C. Liu, Y. Li, T. Peng, S. Luo, Y. Feng, W. Xie, D. Lu, W. Sun, *J. Power Sources* **2020**, *468*, 228393–228401.
- [25] F. Li, J. Gao, Z. He, L. Kong, *ACS Appl. Energ. Mater.* **2020**, *3*, 5448–5461.
- [26] A. Lu, X. Zhang, Y. Chen, Q. Xie, Q. Qi, Y. Ma, D. Peng, *J. Power Sources* **2015**, *295*, 329–335.
- [27] Y. Zhu, Y. Liu, T. Ren, Z. Yuan, *Adv. Funct. Mater.* **2015**, *25*, 7337–7347.
- [28] M. Xu, L. Han, Y. Han, Y. Yu, J. Zhai, S. Dong, *J. Mater. Chem. A* **2015**, *3*, 21471–21477.
- [29] A. C. Ferrari, J. C. Meyer, V. Scardaci, C. Casiraghi, M. Lazzeri, F. Mauri, S. Piscanec, D. Jiang, K. S. Novoselov, S. Roth, A. K. Geim, *Phys. Rev. Lett.* **2006**, *97*, 187401–187405.
- [30] Y. Liu, X. Wang, W. Wan, L. Li, Y. Dong, Z. Zhao, J. Qiu, *Nanoscale* **2016**, *8*, 2159–2167.
- [31] R. Wu, D. P. Wang, X. Rui, B. Liu, K. Zhou, A. W. Law, Q. Yan, J. Wei, Z. Chen, *Adv. Mater.* **2015**, *27*, 3038–3044.
- [32] Z. Zhang, J. Yang, Y. Nuli, B. Wang, J. Xu, *Solid State Ionics* **2005**, *176*, 693–697.
- [33] F. Yang, H. Gao, J. Hao, S. Zhang, P. Li, Y. Liu, J. Chen, Z. Guo, *Adv. Funct. Mater.* **2019**, *29*, 1808291–1808299.
- [34] P. Zhu, Z. Zhang, P. Zhao, B. Zhang, X. Cao, J. Yu, J. Cai, Y. Huang, Z. Yang, *Carbon* **2019**, *142*, 269–277.
- [35] Z. Yi, Y. Liu, Y. Li, L. Zhou, Z. Wang, J. Zhang, H. Cheng, Z. Lu, *Small* **2020**, *16*, 1905301–1905311.
- [36] X. Zhao, W. Wang, Z. Hou, G. Wei, Y. Yu, J. Zhang, Z. Quan, *Chem. Eng. J.* **2019**, *370*, 677–683.
- [37] Y. Li, Y. Hu, M. Titirici, L. Chen, X. Huang, *Adv. Energy Mater.* **2016**, *6*, 1600659–1600668.
- [38] H. Zheng, C. Zhang, Y. Zhang, L. Lin, P. Liu, L. Wang, D. L. Peng, *Adv. Funct. Mater.* **2021**, *31*, 2100783–2100795.
- [39] W. Guo, C. Zhang, Y. Zhang, L. Lin, W. He, Q. Xie, D. L. Peng, *Adv. Mater.* **2021**, *33*, 2103173–2103182.

Manuscript received: June 17, 2022

Revised manuscript received: June 25, 2022

Accepted manuscript online: June 26, 2022

Version of record online: July 29, 2022